ISSN 1999-656X

Iraqi Journal of Applied Physics Letters

VOLUME (4) ISSUE (4) OCTOBER-DECEMBER 2021

Sponsored and Published by
Iraqi Society for Alternative and Renewable Energy Sources and Techniques

Co-published by
American Quality for Scientific Publishing

IRAQI JOURNAL OF APPLIED PHYSICS LETTERS

The *Iraqi Journal of Applied Physics Letters (IJAPLett)* is a peer reviewed journal of high quality devoted to the publication of original research papers from applied physics and their broad range of applications. IJAPLett publishes quality original research letters in physics and its applications in the broadest sense. It is intended that the journal may act as an interdisciplinary forum for physics and its applications. Innovative applications and material that brings together diverse areas of physics are particularly welcome. IJAPLett aims to disseminate knowledge; provide a learned reference in the field; and establish channels of communication between academic and research experts, policy makers and executives in industry, commerce and investment institutions. IJAPLett is a quarterly specialized periodical dedicated to publishing original letters in: Applied & Nonlinear Optics, Applied Mechanics & Thermodynamics, Digital & Optical Communications, Electronic Materials & Devices, Laser Physics & Applications, Plasma Physics & Applications, Quantum Physics & Spectroscopy, Semiconductors & Optoelectronics, Solid State Physics & Applications, Alternative & Renewable Energy, and Environmental Science & Technology.

ISSN (Print): 1999-656X, ISSN (Online): 2958-6488

EDITORIAL BOARD

Oday A. HAMMADI	Asst. Professor	Editor-in-Chief	Molecular Physics	IRAQ
Walid K. HAMOUDI	Professor	Member	Laser Physics	IRAQ
Dayah N. RAOUF	Asst. Professor	Member	Laser and Optics	IRAQ
Raad A. KHAMIS	Asst. Professor	Member	Plasma Physics	IRAQ
Raid A. ISMAIL	Professor	Member	Semiconductor Physics	IRAQ
Kais A. AL-NAIMEE	Professor	Member	Quantum Physics	IRAQ
Haitham M. MIKHLIF	Lecturer	Managing Editor	Molecular Physics	IRAQ
Waleed N. RAJA	Assistant Professor	Member	Radiation Physics	IRAQ
Mahdi S. EDAN	Assistant Professor	Member	Applied Physics	IRAQ
Ali J. MOHAMMED	Assistant Professor	Member	Thin Film Technology	IRAQ
Falah H. ALI	Assistant Professor	Member	Molecular Physics	IRAQ

Editorial Office:
P. O. Box 55259, Baghdad 12001, IRAQ
Website: www.iraqiphysicsjournal.com
Emails: editor@iraqiphysicsjournal.com, editor_ijap@yahoo.co.uk, ijap.editor@gmail.com,

ADVISORY BOARD

Andrei KASIMOV, Professor, Institute of Material Science, National Academy of Science, Kiev,	UKRAINE
Ashok KUMAR, Professor, Harcourt Butler Technological Institute, Kanpur, Uttar Pradesh 208 002,	INDIA
Chang Hee NAM, Professor, Korean Advanced Institute of Science and Technology, Daehak-ro, Daejeon,	KOREA
Claudia GAULTIERRE, Professor, Faculty of Sciences and Techniques, University of Rouen, Rouen,	FRANCE
El-Sayed M. FARAG, Professor, Department of Sciences, College of Engineering, AlMinofiya University,	EGYPT
Gang XU, Assistant Professor, Department of Engineering and Physics, University of Central Oklahoma,	U.S.A
Heidi ABRAHAMSE, Professor, Faculty of Health Sciences, University of Johannesburg,	S. AFRICA
Madis-Lipp KROKALMA, Professor, School of Science, Tallinn University of Technology, 19086 Tallinn,	ESTONIA
Mansoor SHEIK-BAHAE, Associate Professor, Department of Physics, University of New Mexico,	U.S.A
Mohammad Robi HOSSAN, Assistant Professor, Dept. of Eng. and Physics, Univ. of Central Oklahoma,	U.S.A
Morshed KHANDAKER, Associate Professor, Dept. of Engineering and Physics, Univ. of Central Oklahoma,	U.S.A
Qian Wei Chang, Professor, Faculty of Science and Engineering, University of Alberta, Edmonton, Alberta,	CANADA
Sebastian ARAUJO, Professor, School of Applied Sciences, National University of Lujan, Buenos Aires,	ARGENTINA
Shivaji H. PAWAR, Professor, D.Y. Patil University, Kasaba Bawada, Kolhapur-416 006, Maharashtra,	INDIA
Xueming LIU, Professor, Department of Electronic Eng., Tsinghua University, Shuang Qing Lu, Beijing,	CHINA
Yanko SAROV, Assistant Professor, Micro- and Nanoelectronic Systems, Technical University Ilmenau,	GERMANY
Yushihiro TAGUCHI, Professor, Dept. of Physics, Chuo University, Higashinakano Hachioji-shi, Tokyo,	JAPAN

SPONSORED BY
IRAQI SOCIETY FOR ALTERNATIVE AND RENEWABLE ENERGY SOURCES AND TECHNIQUES (I.S.A.R.E.S.T.)
P. O. Box 55259, Baghdad 12001, IRAQ

PUBLISHED BY
AMERICAN QUALITY FOR SCIENTIFIC PUBLISHING INC.
1479 South De Gaulle Ct, Aurora,
CO 80018, United States

IRAQI JOURNAL OF APPLIED PHYSICS LETTERS

ISSN (Print): 1999-656x, ISSN (Online): 2309-1673

INSTRUCTIONS TO AUTHORS

CONTRIBUTIONS

Contributions to be published in this journal should be original research letters, i.e., those not already published or submitted for publication elsewhere, communications or letters to editor.
Manuscripts should be submitted to the editor at the mailing address:

Iraqi Journal of Applied Physics Letters, Editorial Board, P. O. Box 55259, Baghdad 12001, IRAQ
Website: www.iraqiphysicsjournal.com
Email: editor@iraqiphysicsjournal.com, editor_ijap@yahoo.co.uk, ijap.editor@gmail.com

MANUSCRIPTS

Two hard copies with soft Word copy on a CD or DVD should be submitted to Editor in the following configuration:

- **One-column** Double-spaced one-side A4 size with 2.5 cm margins of all sides
- Times New Roman font (16pt bold for title, 14pt bold for names, 12pt bold for headings, 12pt regular for text)
- Manuscripts presented in English only are accepted.
- Total number of words not exceed 2500 words and English abstract not exceed 100 words
- 4 keywords (at least) should be maintained on (PACS preferred)
- Author(s) should express all quantities in SI units
- Equations should be written in equation form (*italic* and symbolic) NOT in plain text
- Tables and Figures should be separated from text and placed in new pages after the references
- Charts should be indicated by the software used for generating them (e.g., Excel, MATLAB, Grapher, etc.)
- Figures and diagrams can be submitted in original colored forms for assessment and they will be returned to authors after provide printable copies
- Only original or high-resolution scanner photos are accepted
- For electronic submission, articles should be formatted with MS-Word software.

AUTHOR NAMES AND AFFILIATIONS

It is IJAPLett policy that all those who have participated significantly in the technical aspects of a paper be recognized as co-authors or cited in the acknowledgments. In the case of a paper with more than one author, correspondence concerning the paper will be sent to the first author unless staff is advised otherwise.
Author name should consist of first name, middle initial, last name. The author affiliation should consist of the following, as applicable, in the order noted:
- Company or college (with department name or company division), Postal address, City, Governorate or State, zip code, Country name, contacting telephone number, and e-mail

REFERENCES

The references should be brought at the end of the article, and numbered in the order of their appearance in the paper. The reference list should be cited in accordance with the following examples:
[1] X. Ning, R. Benford and M.R. Lovell, "On the Sliding Friction Characteristics of Unidirectional Continuous FRP Composites", *J. Tribol. Func. Mater.*, 124(1) (2002) 5-13.
[2] M. Barnes, "Stresses in Solenoids", *J. Appl. Phys.*, 48(5) (2001) 2000–2008.
[3] J. Jones, **"Contact Mechanics"**, Cambridge University Press (Cambridge, UK) (2000), Ch.6, p.56.
[4] Y. Lee, S.A. Korpela and R. Horne, "Structure of Multi-Cellular Natural Convection in a Tall Vertical Annulus", Proceedings of 7th International Heat Transfer Conference, U. Grigul et al., eds., Hemisphere (Washington DC), 2 (1982) 221–226.
[5] M. Hashish, "Waterjet Technology Development", High Pressure Technology, PVP-Vol. 406 (2000) 135-140.
[6] D.W. Watson, "Thermodynamic Analysis", ASME Paper No. 97-GT-288 (1997).
[7] C.Y. Tung, "Evaporative Heat Transfer in the Contact Line of a Mixture", Ph.D. thesis, Rensselaer Polytechnic Institute, Troy, NY (1982).

PROOFS

Authors will receive proofs of papers and are requested to return one corrected copy as a WORD file on a compact disc (CD) or by email. New materials inserted in the original text without Editor's permission may cause rejection of paper unless the handling editor is informed.

COPYRIGHT FORM

Author(s) will be asked to sign the IJAPLett Copyright Form and hence transfer copyrights of the article to the Journal soon after acceptance of it. This will ensure the widest possible dissemination of information.

OFFPRINTS

Authors will receive electronic offprint free of charge and any additional reprints can be ordered.

SUBSCRIPTION AND ORDERS

Annual fees (4 issues per year) of subscription are:
50 US$ for individuals inside Iraq; **200** US$ for institutions inside Iraq;
100 US$ for individuals abroad; **300** US$ for institutions abroad.

Properties of Silicon Diode under Electromagnetic Irradiation

Abdullah H. Ibrahim[1], Faris S. Atallh[1], Musab S. Mohammed[2]

[1] Department of Physics, College of Science, University of Tikrit, Salahaddin, IRAQ
[2] Department of Physics, Faculty of Education, University of Mosul, Nineveh, IRAQ

Abstract
The effect of electromagnetic radiation on the properties of ordinary Si diode with exposed device, studied in was the framework of using visible light sources (VS), of wavelength (630-650nm), wavelength (532±10nm) and wavelength (405nm), i.e. red laser, green laser and blue-violet laser, respectively. As well as ultraviolet (UV) and infrared (IR), where sources with wavelengths (395nm) (850 nm) were used, respectively.As well as to using transistor (2N3773) as diode, by using base and emitter pins. Then we calculate and scheme the V-I in-state forward bias characteristic curve for the diode in two states with and without the effect of radiation, and compared between them. Where we getted to barrier potential is equal to (13.548 V) for exposed diode device without effect for electromagnetic radiation where (12.885 V), (12.626 V), (11.818 V), (13.425 V) and (13.366 V), the first three values are for visible light, the fourth value for ultraviolet radiation, and the fifth value for infrared radiation, According to the order of wavelengths above. The frontal resistance was also calculated from the curve for the knee region, and the regions before and after the knee.

Keywords: Radiation; Diode; Exposed Device; Characteristic Curve; Visible light; Ultraviolet; Infrared
Received: 20 July 2020; **Revised:** 15 August 2020; **Accepted:** 12 September 2020; **Published:** 1 October 2021

1. Introduction

Numerous researchers have looked into semiconductor devices' radiation effect. Numerous papers that offer experimental data on the impact of radiation on silicon devices have been published [1-3]. Irradiation has a significant impact on the characteristics of semiconductor diodes and other semiconductor devices. The V-I curve is altered as a result, changing both branches. The type of semiconductor, the device's design, and the operating circumstances all affect how big such changes will be. As a result, the degree of forward V-I characteristic deformation and changes in reverse characteristics can occasionally be used to predict the radiation stability of diodes. Consequently, it is challenging to develop a comprehensive criterion for the radiation, stability of diodes, in contrast to transistors [4]. The maximum allowable saturation current or its permissible percentage rise is often the radiation stability criterion for germanium diodes, for which the reverse branch experiences the majority of changes. The criteria for radiation stability for silicon diodes also include a specific maximum allowable change, either in the voltage drop on the forward branch or the forward resistance, as these parameters are affected by radiation and exhibit changes in the forward V-I characteristics [4]. Electronics and their parts and components have become increasingly popular in recent years. Evidently, there is a chance that injecting external electromagnetic fields will cause the electrical system to produce unsettling indications. The danger posed by electromagnetic, pulse radiation, which might inadvertently cause or purposely, because of their proximity to electronic devices, pair into the high-frequency environmental signal-typically in the need for a microwave to get more attention. It would be tragic and unthinkable if the electronic systems malfunctioned or were destroyed. The semiconductor devices could sustain long-term harm from the electromagnetic radiation [5-10].

2. Characteristics Curve of Diode

With the exception of a very small reverse current, reverse bias effectively stops current from flowing through a diode. As long as the

 © All Copyrights are reserved

p-n junction's breakdown voltage is less than or equal to the reverse-bias voltage, reverse bias prohibits current flow [13]. Current flows through a diode when a forward−bias voltage is put across it. The forward current is known as "I_F" and is referred to as such. Using the resistor, the forward current is constrained to a level below which the diode won't become overheated and suffer damage. When there is zero voltage, there is no forward current, over the diode. Raising the forward-bias voltage causes a steady increase in the forward current and voltage across the diode. The forward-bias voltage that is dumped over the limiting resistor is only partially applied to it. Up until the voltage across the Si diode reaches roughly 0.7V (barrier potential of Si), the forward current begins to rapidly increase when the forward-bias voltage is increased [13].

Although only when the diode's voltage increases little by little over 0.7 V as a forward−bias voltage is increased, a current keeps rising quite quickly. Due to the voltage drop across the internal dynamic resistance of the semiconductive material, the diode voltage has only slightly increased above the barrier potential [13].

For a given change in voltage. Because the current increases so little below the curve's knee, the resistance is highest ($R_f = \Delta V_F/\Delta I_F$). The resistance starts to drop around the curve's knee, and is at its lowest above the knee, where there is a significant for a specific change in voltage, the change in current [13].

3. Results and Discussion.

Figure (1) displays the circuit diagram for the operation, which includes a variable power supply, a voltmeter, an ammeter, a 470Ω resistor, (2N3773) transistor, electromagnetic radiation sources and wires.

Electromagnetic radiation's impact on the characteristics of ordinary Si diode with the exposed device, was first studied without any effect except at pre-illumination of the laboratory room, V_F and I_F starting from 0.001V and 0.1 μA at zero voltage bias, as shown in Fig. (3a) where the barrier potential approximately equal to 13.548V. The resistance of forward of a diode is 9089.233 kΩ before the knee of the curve's area, and after it is 1.825 kΩ. Figure (2b) shown the diode's V-I characteristic curve under effect the ultraviolet of wavelength (395 nm) whose agree with the diode's V-I characteristic curve without effect, where V_F and I_F starting from 0 V and 1.1 μA at zero voltage bias, the barrier potential approximately equal to 13.425 V.

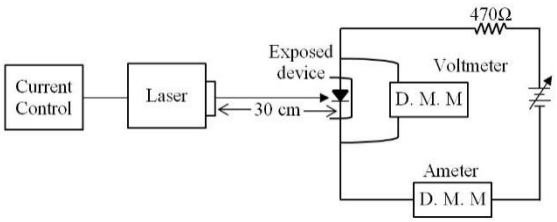

Fig. (1) The circuit diagram of the operation

As well as the effect of infrared of wavelength (850 nm), with barrier potential approximately equal to 13.366 V, we note that the characteristic curve up to the current axis, by increasing the voltage even reaches approximately barrier potential the region of the knee become consist, that also happen for visible light of wavelength (630-650 nm), and power of sores 5 mW. The barrier potential approximately equal to 12.885 V for last effect. Also from the Fig. (2b), we note that both infrared and ultraviolet radiation do not affect the shape of the curve, as they are completely compatible with the original curve without any effect, where the effect is on the voltage barrier and the forward resistance of the curve, before and after the knee, while the effect of the red laser light is also in the shape of the curve, where the knee area has a wider arc than it is in the previous effects.

Now the resistance of forward of a diode for effects it find in Fig. (2b), we can calculated for region before the knee region it equal to 6874.601 kΩ, 1030.842 kΩ and 541.665 kΩ for ultraviolet, infrared and laser of red light, respectively, but the resistance of forward of a diode after the knee region for ultraviolet is 2.137 kΩ, infrared is 0.441 kΩ and laser of red light is 0.885 kΩ.

 © All Copyrights are reserved

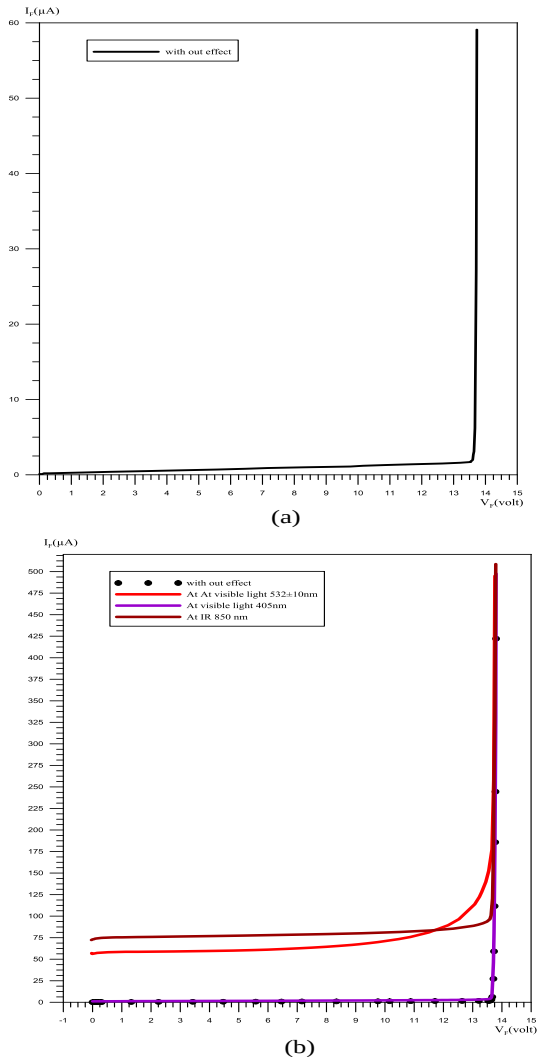

Fig. (2) Electromagnetic radiation has an impact on the relationship between voltage and current in a forward-biased diode

In Fig. (3) comparison between effect of lasers green light and blue-violet light with general state at power of source 100 mW, the barrier potential approximately equal to 12.626 V and 11.818 V for blue-violet light and green light respectively. The resistance of forward of a diode for effects it find in Fig. (3) is 59.737 kΩ and 65.789 kΩ for blue-violet light and green light respectively, for region before the knee region, and after region the knee 0.192 kΩ and 0.117 kΩ. The effect of electromagnetic radiation for all sources it used was on the barrier potential and the resistance of forward of a diode before the knee region, where we have noticed that the barrier voltage is less than what it is in the normal case, as well as the forward resistance of the diode in the knee region and before and after the knee region, except for one case in which the front resistance is higher than the normal case, which is the region after the knee under the effect of ultraviolet radiation.

The V_F and I_F in Fig. (3) starting from -0.2V and 366.2 μA for green light, and -0.414V and 1209 μA for blue-violet light at zero voltage bias.

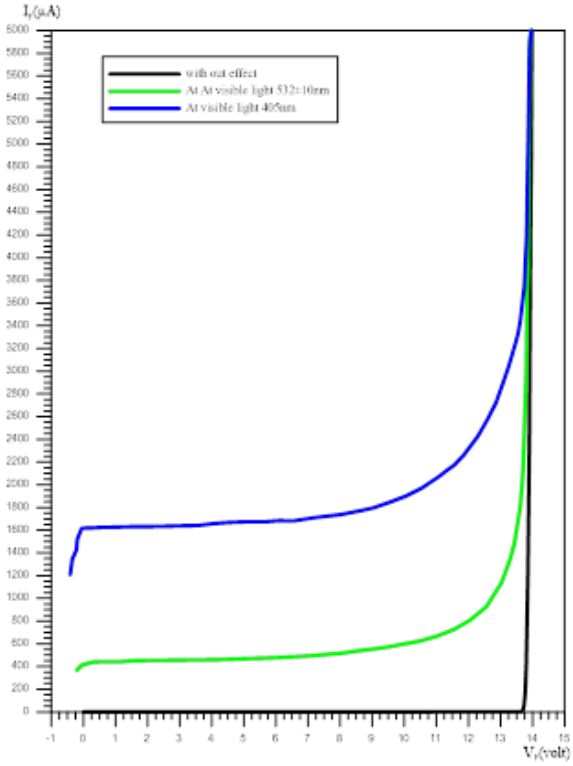

Fig. (3) Electromagnetic radiation has an impact on the relationship between voltage and current in a forward-biased diode

4. Conclusions

In this paper, the effects of UV, IR and laser of red light on the curve agreement with the normal case in terms of behavior, where the behavior was different. The effect of electromagnetic radiation was changed the barrier potential of the p-n junction, where this change can be considered as a measure of wavelength. As well as to the sliding of the bias current to up on the current axis, which magnitude varies from one wavelength to another. This is another parameter that can be used to measure or detect electromagnetic radiation.

References

[1] N.A. Hastas et al., "Effects of gamma-ray irradiation on polycrystalline silicon thin-film

 © All Copyrights are reserved

transistors", *Microelectron. Reliab.*, 43(1) (2003) 57.
[2] S. Zhang et al., "The effects of operating bias conditions on the proton tolerance of SiGe HBTs", *Solid-State Electron.*, 47(10) (2003) 1729.
[3] S.A. Kamh and F.A.S. Soliman, "Environmental conditions effect on characteristics of some unijunction and bijunction semiconductor devices", *Nucl. Instrum. Meth. Phys. Res. A*, 564 (2006) 463-470.
[4] R.A. Ismail et al., "Characterization of Si p-n Photodetectors Produced by Laser-Induced Diffusion", *Int. J. Mod. Phys.*, 19(31) (2005) 4619-4628.
[5] O.A. Hamadi and K.Z. Yahiya, "Optical and electrical properties of selenium-antimony heterojunction formed on silicon substrate", *Sharjah Univ. J. Pure Appl. Sci.*, 4(2) (2007) 1-11.
[6] V.S. Vavilov and N.A. Ukhin, "Radiation Effects in Semiconductors and Semiconductor Devices", Library of Congress Catalog Card Number 76-17409 (1977) Ch. 2.
[7] C. Kopp and R. Pose, "The Impact of Electromagnetic Radiation Considerations on Computer System Architecture", Dept. of Computer Science, Monash University, Clayton, Victoria (Australia).
[8] R.A. Ismail et al., "Full Characterization at 904nm of Si p-n Junction Photodetectors Produced by LID Technique", *Eur. Phys. J.: Appl. Phys.*, 38 (2007) 197-201.
[9] S. Krishnan, G. Sanjeev and M. Pattabi, "Electron irradiation effects on the Schottky diode characteristics of p-Si", *Nucl. Instrum. Meth. Phys. Res. B*, 266 (2008) 621-624.
[10] O.A. Hamadi, B.A.M. Bader and A.K. Yousif, "Electrical Characteristics of Silicon p-n Junction Solar Cells Produced by Plasma-Assisted Matrix Etching Technique", *Eng. Technol. J.*, 28 (2008).
[11] High Power Microwave Technology and Effects, University of Maryland Short Course Presented to MSIC Redstone Arsenal, Alabama August 8-12, 2005.
[12] S.M. Hwang, J.I. Hong and C.S. Huh, "Characterization of the susceptibility of integrated circuits with induction caused by high power microwaves", *Prog. in Electromag. Res. PIER*, 81 (2008) 61-72.
[13] A.A.K. Hadi and O.A. Hamadi, "Optoelectronic Characteristics of As-doped Si Photodetectors Produced by LID Technique", *Iraqi J. Appl. Phys. Lett.*, 1(2) (2008) 23-26.
[14] V.V. Shurenkov, "On the physical mechanism of interaction of the microwave radiation with the semiconductor diodes", *Adv. Mater. Res.*, 1016 (2014) 521-525.
[15] O.A. Hammadi, "Photovoltaic Properties of Thermally-Grown Selenium-Doped Silicon Photodiodes for Infrared Detection Applications", *Phot. Sen.*, 5(2) (2015) 152-158.
[16] X. Fei, C. Bing and L. Chenglong, "Damage efficiency research of PCB components under strong electromagnetic pulse", *Appl. Mech. Mater.*, 130-134 (2012) 1383-1386.
[17] J.U. Lee, P.P. Gipp and C.M. Heller, "Carbon Nanotube P-N Junction Diodes", *Appl. Phys. Lett.*, 85(1) (2004) 145-147.
[18] V.V. Shurenkov and V.S. Pershenkov, "Electromagnetic Pulse Effects and Damage Mechanism on the Semiconductor Electronics", Electron. Energet., 29(4) (2016) 621-629.
[19] T.L. Floyd, **"Electronic Devices"**, 10th ed., Conventional Current Version, Prentice Hall (Boston 2017), Ch. 2.
[20] O.A. Hammadi, "Characteristics of Heat-Annealed Silicon Homojunction Infrared Photodetector Fabricated by Plasma-Assisted Technique", *Phot. Sen.*, 6(4) (2016) 345-350.

 © All Copyrights are reserved

X-Ray Diffraction Analysis of Titanium-Cobalt Alloys Prepared by Plasma Sputtering

Zainab T. Abdulhamied, Shahlaa Jomaa, Aqeel F. Hassan

Ministry of Science and Technology, Baghdad, IRAQ

Abstract

In this study, sputtering in plasma technique was used to enhance the yearly corrosion average of alumina to be about $2.21x10^{-4}$ mpy on Ti-20%Co alloy. This alloy (Ti-Co) is popularly used for surgical implant because it has good mechanical properties, high degree of biocompatibility, bioinert and osseo-integrations with bones. This research is focusing on different sputtering parameters such as the discharge voltage, sputtering time and gas pressure. A good result was found when a 1200 V is applied on the electrodes for 4 hours under $4x10^{-3}$ mbar argon gas pressure. The structural characteristics of the alloy were studied before and after coating using x-ray diffraction (XRD) technique while the morphology of the specimen surface was investigated by the optical microscopy. The electrochemical tests of the Ti-20%Co alloy were also performed before and after coating in simulated body fluids. The average corrosion rate of alloy before coated was $1.98x10^{-2}$ mpy, while the average corrosion rate after coted Al_2O_3 was about $2.21x10^{-4}$ mpy at 1200 V.

Keywords: Plasma sputtering; Ti-Co alloys; Corrosion; Ceramics; Biomaterials; Biomedical applications
Received: 02 March 2020; **Revised:** 05 April 2020; **Accepted:** 12 April 2020; **Published:** 19 April 2020

1. Introduction

The ceramic science studies the features or the characteristics of an organic metallic solid except the metals and alloys, it is made up in high temperature to use it in different fields [1]. Ceramic includes an inorganic metal materials that form clay, mud and found as oxides. Ceramic products can be obtained by technique of powder not from its fusion. This product is considered a difficult step because it needs a high temperature (more than 2000°C) and cannot put Ceramic fusion in a mold that has a limited temperature [2].

When we heating the aluminum hydroxide under 400°C y- aluminum oxide. It seems white smooth powder and disintegrates in acids and moves to phase α-aluminum when heating to it under 950°C. Also, that y-aluminum characterize of its good portability of absorption so this is why it is used during operations and removal colors of solutions [8,9]. Surface modifications of materials provide the base for achieving specific material properties for specific applications. The main advantage of laser surface modification is the ability to improve the properties of different materials [12]. The performance and applications of biomaterials in biological systems are of critical importance for the development of biomedical implants and tissue engineering. There are numerous biomaterials that can be used in the human body, such as metals e.g. stainless steel, cobalt alloys, titanium alloys), ceramics (aluminum oxide, zirconia, calcium phosphates), and synthetic and natural polymers [13]. Table (2) summarizes the medical and biomedical applications of some ceramic materials.

Titanium is a reactive material and has an very high affinity for oxygen, which means that the protective oxide film forms spontaneously and instantly and its disruption or damage is repaired immediately [9], if the metal is in the presence of air or oxidizing media, as is the case in a biological system when a bio-liquid surrounds the metal [17].

Table (2) Medical and biomedical applications of some ceramic materials [3]

Ceramic		Applications
Alumina	Al_2O_3	Cutting tools, dies, wear, resistant parts and coating, oxidation barriers, bearing surfaces, high temperature components, turbine parts, hip implants, body armor, radiation shielding.
Silicon Carbide	SiC	
Silicon Nitride	Si_3N_4	
Zirconium	ZrO_2	
Boron Nitride	BN	

 © All Copyrights are reserved

2. Materials and methods

In the sputtering system used in this work, the vacuum chamber has a cylindrical shape and made from stainless steel. The chamber two electrodes (cathode and anode). The plasma chamber is evacuated down by a rotary pump to reach about 10^{-2}mbar, and by a turbo pump to achieve pressure about 10^{-4} mbar. Using the Pirani and Penning gauges attached to the top cover of chamber through a hole measuring by a needle-shaped tubes and it could be controlled with the amount of gas and determining pressure inside plasma chamber. The power supply has been used which is locally made with continuous electrical current about 4 kV.

Ti-20%Co is used in this research cut a rectangular using metal cutting device with (10×10×2 mm) dimensions.

For the facility of grinding, polishing and electrochemical studies the specimens are mounting and putting in a model uniform with 25mm diameter. A wire from material of Brass has been reached for the specimens that are preparing for the corrosion test with a silver past material to contact between the specimen and potentiostatic through corrosion test and total insulation of wire from the corrosion region.

The operation of wet grinding has been done with water as it is considered a cooling liquid to prevent from happening more stressful operations for the specimen as a result of high temperature and by using Sic grinding paper with different grits started from 120 grits, and continuing to 320, 500 and 600 grits to get flat and scratch free surface. Then polishing step using a rolling disk covered with a silk cloth and an oiled material is the Silica suspension and with particle size 0.5 mic to obtain a mirror polished surface. cleaning procedures is used for mirror surface with acetone and by using ultrasonic cleaning system then the specimen is washed with a dropped water.

The sputtering system consists of an inert gas (argon) to produce ions and target material, which is alumina (Al_2O_3) and zirconia (ZrO_2). The plasma material is putting inside the chamber and applied voltage about 1200 V, inter-electrode distance is 4 cm, and pressure is $4x10^{-2}$ mbar are the operation conditions of the system for this project. Table (3) shows the most important operation parameters of dc sputtering system.

Particles directing speedily towards the target, and the argon ion will win energy that is needed to separate the atoms from the target material. The distance between the target and plasma material identified previously. The engineering design in which the Argon ions revel the alumina material and collide with the atoms.

Table (3) Sputtering system under search (DC-Sputtering)

The type and operating value	Specifications
Alumina	The target
1 keV	The target voltage
Argon gas	The sputtering gas
1 cm	Radius of target
4 cm	The distance between the target and the ground
$4x10^{-2}$ mbar	The gas target pressure
300 K	The gas temperature

To study a specific structure of the alloy by using etchant solution consists of 10 ml of HCl, 5 ml of HNO_3 and 15ml of water. When specimen rub for 5 s followed by the operating washing and drying, then the important details exposed by this step.

Surface morphology of the specimens was examined by using reflecting photographic microscope Nikon type 120-Japa With a megascopic power varying between (50-1000X) provided with a digital camera type DMX12000F.

For the purpose of examining the phases that forms by Ti-20%Co alloy and these phases are contacting with corrosion of alloy before and after coating by using X-ray diffraction facilities (Shimadzu LabX XRD-6000) and the target mineral that is used in the x-ray tube is copper and diffraction angle (2θ) is ranging through 20-80°.

The corrosion average is investigated using the Tafel extrapolation method. The purpose of this method to obtain polarization data. the electrochemical system consists from Potential Stress device the cell measurements and electrodes. The specification of the cell used in this test is a spherical shape with a

 © All Copyrights are reserved

capacity 1liter and made from a glass material. The cell also contains five different necks to put the electrodes on it.

The SBF solution which is laboratory made was used as a medium to investigate the corrosion of alloy before and after sputtering. The solution was made by adding it´s chemical composition as shown in table (4) respectively the ingredients melted in a glass beaker by using the ionic water with mixing for one hour, then the pH was adjusted to 7.4 to simulate body fluid by adding a several drops of HCl acid to the solution.

Table (4) Chemical composition of SBF solution

NO.	Constituent	Weight(gm/l)
1	NaCl	0.700
2	KCl	1.200
3	K_2HPO_4	0.200
4	$NaHCO_3$	1.500
5	Na_2HPO_4	0.260
6	KSN	0.330
7	Urea	0130

3. Discussion

For the purpose of studying the influence of the sputtering with the ceramic materials which are biologically effective in the behavior of the corrosion of Ti-20%Co alloy. Sputtering is done on many specimens which are selected from the alloy with the alumina material. We are going to discuss the results of analyzing the elements which contain alloy, the phases that are formed by x-ray diffraction (Microscopic examination) and also the results of electrochemical measurements before and after sputtering.

The results of XRD show in Fig. (1) of main alloy, Three diffraction peaks after compare it with the results (that are published from the National Center of the Diffraction Information), the phases former of the Ti-20%Co alloy appears that the base phase formed is β Ti (011) phase with (bcc) crystal structure [12]. Also that two phases regards alloy appear, first (Ti_2Co) with (bcc) crystal structure, we notice that this phase is controlled after β Ti reflections (331), (511), (440), (751), respectively the result of diffraction shows a small phase appears hexagonal (α-Ti) with the reflections (100) and (103) in the crystal structure of the alloy.

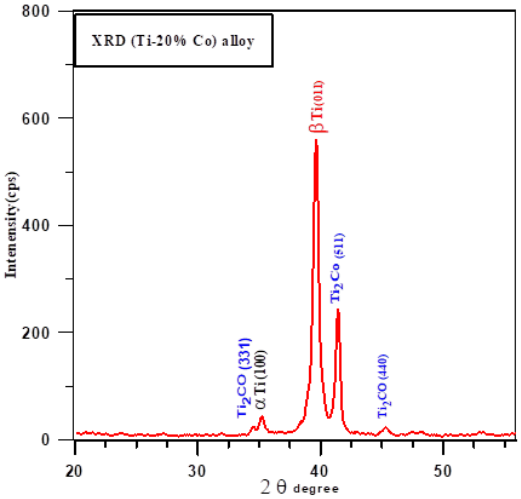

Fig. (1) Phases of alloy Ti-20% Co before coating

Figures (2) and (3) show the diffraction results of coating alloy treated by sputtering with the alumina material and thickness of 0.41 and 0.3 mm, respectively. We notice phases of coating layer with reflections (119), (018), (024), (202), (113), (110), and (104). Otherwise, the reason of the reflections appearing of the Ti and Ti-Co is the inaccuracy precipitate and some exposed areas exist which causes the appearing the reflections of Ti_2Co (511), β-Ti(011) [12,14].

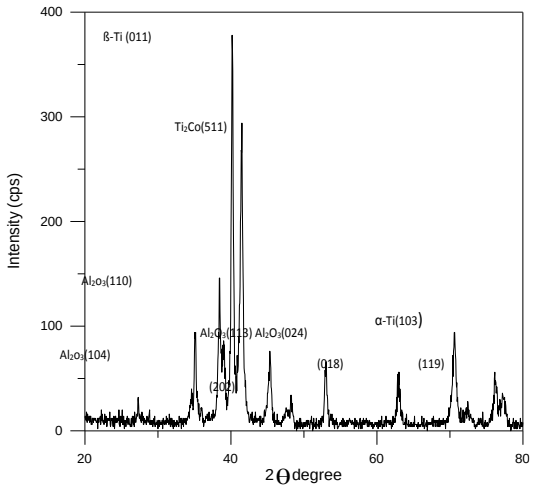

Fig. (2) Phases consist of alloy coating with Al_2O_3 and thickness 0.41 mm

 © All Copyrights are reserved

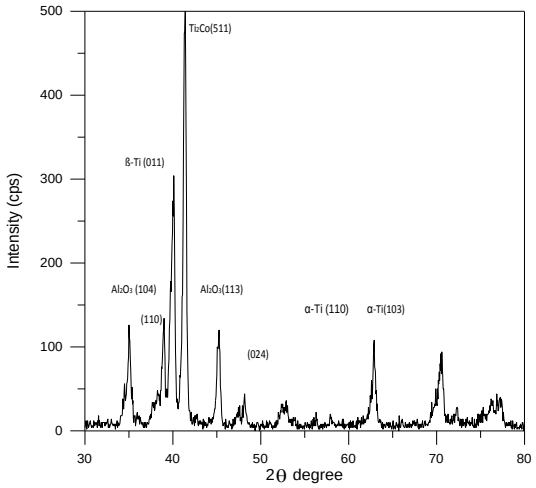

Fig. (3) Phases of alloy coating with Al_2O_3 and thickness 0.3 mm

4. Conclusions

The results indicated that Ti-Co developed a more stable passive layer than the other alloys. This is due to thick Al_2O_3 layers that help create a passive layer that is more resistant to corrosion. The results show the clearly increasing in the sputtering voltage leads to increasing the layer thicknesses at the same time, all optical microscopic pictures shows homogenous Al_2O_3 thick films on Ti-Co alloy surface, also we found the base structure which formers from β-Ti with cubic body center in white color with deep color for α-Ti phases.

References

[1] D. Bochenek, "Advanced Ceramic Materials with Functional Properties", *Materials*, 15 (2022) 6439.

[2] J.R. Kelly and P. Benetti, "Ceramic materials in dentistry: historical evolution and current practice", *Australian Dent. J.*, 56(1) (2011) 84-96.

[3] P.K. Davies and R.S. Roth, "Chemistry of Electronic Ceramic Materials", NIST Special Publication, 804 (1990).

[4] R. Elo, S. Jacobson and T. Kubart, "Tailoring residual stresses in CrN_x films on alumina and silicon deposited by high-power impulse magnetron sputtering", *Surf. Coat. Technol.*, 397 (2020) 1259.

[5] B. Kohlhauser et al., "How microalloying of the Al target can improve process and film characteristics of sputtered alumina", *Surf. Coat. Technol.*, 393 (2020) 125762.

[6] A.M. Titu, B. Miao and A.B. Pop, "Special Issue: Surface Modification of Magnesium, Aluminum Alloys, and Steel", *Coatings*, 12 (2022) 1349.

[7] D.R. Unune, G.R. Brown and G.C. Reilly, "Thermal based surface modification techniques for enhancing the corrosion and wear resistance of metallic implants: A review", *Vacuum*, 203 (2022) 111298.

[8] N. Llorca-Isern and O. Rius-Ayra, "Specia Issue: Surface Modification of Metals and Alloys" *Coatings*, 11(2) (2021) 260.

[9] N. Cui, S. Chen and T. Xu, "The Microstructure, Mechanical Properties, and Corrosion Resistance of a Novel Extruded Titanium Alloy", *Metals*, 12 (2022) 1564.

[10] X. Geng, J. Jiang and X. Zhang, "Corrosion Behavior of $Mg_{-x}Gd_{-1}Zn_{-0.4}Zr$ Alloys with Different Gd Additions for Biomedical Application", *Metals*, 12(10) (2022) 1763.

[11] H.N. Åhman and F. D'Elia, "Microstructural Origins of the Corrosion Resistance of a Mg-Y-Nd-Zr Alloy Processed by Powder Bed Fusion–Laser Beam", *Front. Bioeng. Biotechnol.*, 01 July 2022, doi: 10.3389/fbioe.2022.917812.

[12] J. Sypniewska, "Influence of Laser Modification on the Surface Character of Biomaterials: Titanium and Its Alloys - A Review", *Coatings*, 12 (2022) 1371.

[13] B.T. Lee, A.K. Gain and H.Y. Song, "Fabrication of Porous Al_2O_3 and ZrO_2 Ceramics and Evaluate their Biocompatibility", *Euro. Cells Mater.*, 11(Suppl. 1) (2006) (page 47).

[14] S. Chitra et al., "Strategies of Bioceramics, Bioactive Glasses in Endodontics: Future Perspectives of Restorative Dentistry", *BioMed Res. Int.*, Volume 2022, Article ID 2530156.

[15] K.D. Weltmann, "Biomedical applications of atmospheric pressure plasma", *Chem. listy*, 102 (2008) 1450-1451.

[16] X. Liu, P. Chu and C. Ding, "Surface modification of titanium, titanium alloys, and related materials for biomedical applications", *Mater. Sci. Eng. R*, 47 (2004) 49-121.

[17] F. Almeraya-Calderón and J.M. Jáquez-Muñoz, "Corrosion Behavior of Titanium and Titanium Alloys in Ringer´s Solution", *Int. J. Electrochem. Sci.*, 17 (2022).

 © All Copyrights are reserved

Structural Properties of Nanocrystalline MgO:TiO_2 Thin Films Prepared by Sol-Gel Method

Amel S. Suber, Hanaa K. Khalaf, Seham Z. Abbas, Mohammed E. Ismael

Directorate of Materials Research, Ministry of Science and Technology, Baghdad, IRAQ

Abstract

In this paper, the structural properties of MgO and MgO:TiO_2 nano-films fully grown on clean substrates of quart use technique of sol-gel (dip-coating) are studied. It should be noted that the thickness of the deposited film was about (250) nm. The films were heated in air at 550 °C for 3 hours. Properties structural were identified with various conditions of preparation such as concentration of TiO_2 doping (pure, 3% & 5%) films analyzed by x-ray diffraction (XRD), scanning electron microscopy (SEM), and atomic force microscopy (AFM). The results determined the size of the particle of the prepared films that were dropped with high concentrations of TiO_2 dopants, and some properties of the structure were varied by adding TiO_2 levels as dopants. Films are preferentially oriented to forever (200) directions. The results showed the size of the particle decreased and dropped at a high concentration of doping.

Keywords: Thin films; Sol-gel; magnesium oxide; Titanium dioxide; Gas sensors

Received: 2 July 2020; **Revised:** 5 August 2020; **Accepted:** 12 September 2020; **Published:** 1 October 2021

1. Introduction

During the past few years, the synthesis of nanostructure metal oxide materials has alarmed researchers due to its potential applications. In the current years, scientists have concentrated more on the production of MgO nanoparticles due to their new applications in advanced technologies [Diachenkoa et al., 2016]. Metal oxides are very important materials of technology for use in electronics and devices of photonic. (MgO) is a very convenient filter for applications of insulation owing to its low capacity of heat and high melting point[Obeid et al., 2017], pollutant absorbents, and gas sensor[Fathi et al., 2014], These days, its use might be more intriguing. Due to their potential use as heterogeneous catalysts and supports for metal nanoparticles in electronic devices, insulating metal oxides have received a lot of attention recently [Suresh, 2014].

The aim of this search is to find, the influence of the doping of TiO_2 on the structure, optical, and sensing properties of MgO thin films by using sol-gel technique.

2. Experimental Details

In this paper, the route of the inorganic precursor was selected to fabricate MgO nano-doped with TiO_2 thin films. In the first step, MgO was prepared by dissolving 8.3 g Mg-acetate tetrahydrate $(CH_3COO)_2Mg{\cdot}4H_2O$) (99%) in 30 ml of methanol. Nitric acid is added to the solution while stirring as a catalyst. The stirring was continued for 1 hour at room temperature to obtain a clear and homogeneous solution. In the second step, TiO_2 was prepared by using $Ti\{OCH(CH_3)_2\}_4$, the ethanol C_2H_5OHEtOH and acetic acid CH_3COOH as a catalyst, Obtained of all materials were from (Sigma Aldrich) with a purity of 99%. A gel solution was attained by dissolving 3.15 ml of TIP in 25 ml of ethanol and 5 ml of acetic acid, and for 1 hour was the solution stirred. In the third step, add TiO_2 to MgO solution with volume ratio (V/V) of 3% and 5% with stirred at 60°C for 30 minutes to obtain a homogenous MgO aqueous solution which leaves to 24 hours at room temperature before the deposition process. Then, Pure and TiO_2, doped MgO was deposited on quartz substrate using dip coating technique and then dried on a hot plate for 25 min at 100°C. Finally, the films were annealed with a furnace for 3 hours at 550°C to obtain nanocrystallization of MgO.

Structure crystal analysis of MgO films based on and using a SHIMADZU XRD system with CuKα1 irradiation with λ=1.54Å.

 © All Copyrights are reserved

The size of the crystal was calculated using the equation of Scherer [Patterson,1939]:

$$D = k\lambda / \beta \cos\theta \quad (1)$$

where k is a constant to be booked as 0.9, λ is the wavelength of x-ray (1.54 Å), β is the full-width at half maximum (FWHM), and θ is the diffraction or Bragg's angle of the XRD peak

The shapes of the resulting films were described by a CSPM- 5000 atomic force microscope (AFM) and VEGA TEN SCAN scanning electron microscope (SEM). Optical transmittance and absorbance measurements were performed using a SHIMADZU 1800 dual-beam UV/VISIBLE spectrophotometer in the wavelength range of 300-1000 nm.

3. Results and Discussion

Figure (1) displays the diffraction of x-ray diffraction patterns of TiO_2-doped MgO films at different concentrations of TiO_2 doping (pure, 3, and 5 wt.%), on quartz substrates annealed at 550°C. The XRD patterns reveal strong and sharp (200) and (220) diffraction peaks respectively indicating the formation of MgO.

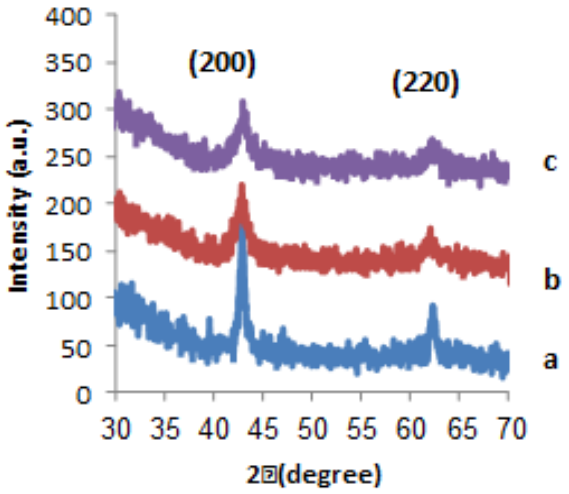

Fig. (1) XRD patterns of MgO films at different doping levels of TiO_2 (a) pure, (b) 3%, and (c) 5%

All films are polycrystalline with a cubic structure. The TiO_2-phase compound at these peaks could not be confirmed by XRD due to small levels of TiO_2 doping. The crystallite size was calculated using Eq. (1) to be 35.2, 22.4 and 12.2 nm for doping levels of 0, 3, and 5 wt.%. of TiO_2 doping, respectively. It is clear that the crystallite size decreases with the TiO_2 doping level due to the difference in molecular size between MgO and TiO_2, which can cause a slight lattice disruption and these results are in agreement with [Güney H, and Iskenderoglu, 2018; Shaush et al., 2020].

Figure (2) reveals the 3D AFM profiles of pure and doped MgO thin films for different concentrations of TiO_2 (pure, 3 and 5 wt.%). The regular size of the grain of the doped and pure MgO films is measured from AFM results using software to be 90-60nm. The AFM results show that by the TiO_2-doped MgO thin films were rougher than the pure film, and the grain size became smaller. This result is consistent with [Wojcienszak, et al (2017)].

Fig. (2) 3D AFM images of MgO films at various concentrations of doping with TiO_2 (a) pure, (b) 3%, and (c) 5%

Figure (3) shows SEM images indicating the surface morphology of pure and TiO_2-doped MgO thin films on quartz substrates. These images clearly show that the formed particles are spherical. Moreover, samples of MgO-TiO_2 materials that did not undergo

 © All Copyrights are reserved

calcination contain relatively fine primary particles attached and tend to agglomerate. The calcination process caused some changes in the particles' shape and size. Particles appeared with irregular shapes and relatively large sizes, with less tendency to form larger agglomerates. This fact is probably related to the significant removal of water (humidity) from the samples due to heat treatment. The presence of physically bound water in the uncalcined samples allowed their particles to agglomerate, and they are dense with little porosity without any cracks. The grain sizes obtained from the SEM images are 95.2, 80.3, and 70.11 nm for pure, 3 wt.% and 5 wt.% doped samples, respectively. These results are in agreement with the preceding findings [Bais & Pathak, 2015). Because the film has a wide surface area that may be exposed to the gas, this form of growth aids to use these films as gas sensors. Particle size as determined by AFM and SEM is larger than that determined by XRD as indicated in table (1).

Table (1) Variation of size of grain of MgO from AFM, SEM, and XRD at different doping of TiO_2

		AFM Grain Size (nm)	SEM Grain Size (nm) SEM	XRD Crystallite Size (nm)
TiO_2 doping concentrations	Pure	90	95.2	35.2
	3%	79.5	80.3	22.4
	5%	60	70.11	12

This explains why SEM and AFM showed particle aggregation but XRD showed average crystallite size. The results of XRD, AFM and SEM may be explained by the fact that particles with free surface energies greater than those of elementary particles tend to aggregate more quickly and develop into packing machine granules.

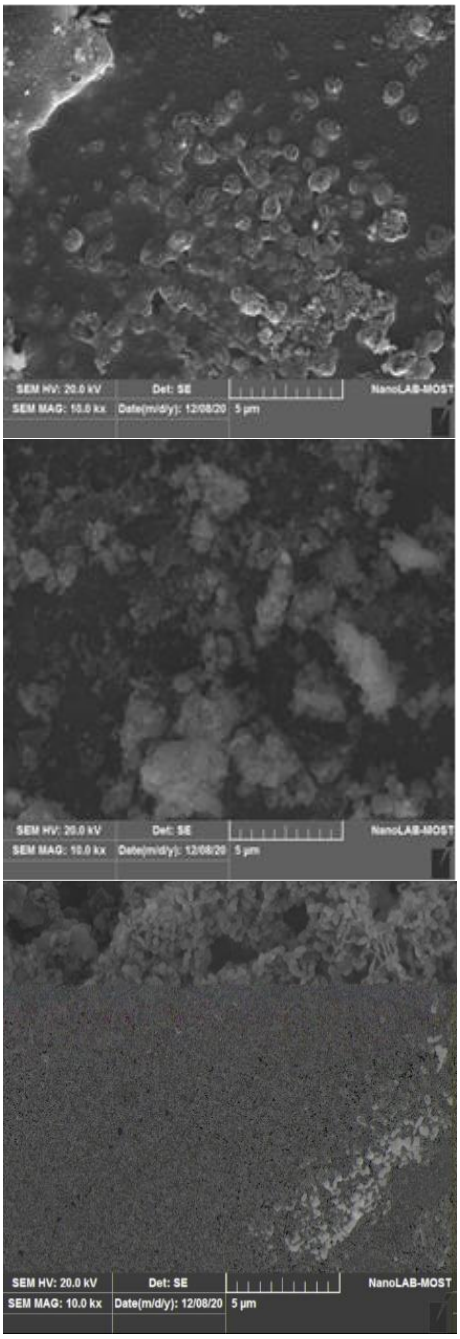

Fig. (3) SEM images (top view) of MgO films at various doping concentrations with TiO_2 (a) pure, (b) 3%, and (c) 5%

4. Conclusion

Structural characterization showed that all films are polycrystalline and the degree of crystallinity decreases with increasing TiO_2 doping level. All samples showed high transmittance in the visible region, which decreases with increasing TiO_2 doping level. The values of the optical band gap are noticed to decrease from 4 to 3.68 eV at higher TiO_2 doping levels. The results of SEM and AFM

 © All Copyrights are reserved

display that the grain size decreases as the doping level is increased.

References

[1] A.O. Mousa, N.A. Nema and H.T. Saleem, "Study of structural and optical properties for MgO films prepared by using chemical spray pyrolysis technique", MSAIJ, 14(11) (2016) 426-434.

[2] Y. Akaltun et al., "The effect of wettability on corrosion resistance of oxide films produced by SILAR method on magnesium, aluminum and copper substrates", *Surf. Coat. Technol.*, 292 (2016) 121-131.

[3] S.M.H. Al-Jawad, A.K. Elttayf and A.S. Saber, "Studying Structural, Optical, Electrical, and Sensing Properties of Nanocrystalline SnO_2:Cu Films Prepared by Sol-Gel Method For CO Gas Sensor Application at Low Temperature", *Surf. Rev. Lett*., 24(7) (2017) 1750110.

[4] A. Alavi and A. Morsali, "Syntheses and characterization of $Mg(OH)_2$ and MgO nanostructures by ultrasonic method", *Ultrason. Sonochem.*, 17 (2010) 441-446.

[5] A.M. Alper, **"High-Temperature Oxide Part II: Oxides of Rare Earths, Titanium, Zirconium, Hafnium, Niobium and Tantalum"**, Academic Press (NY, 1970).

[6] S. Bais and R.K. Pathak, "Corrosion and Structural studies of Galvanostatically Electrodeposited ZnMgO Thin Films", Int. J. Sci. Res., (2015) 1163-1168.

[7] N. Chaouch, S. Benramache and S. Lakel, "Synthesis and Characterization of Physical Properties of MgO Thin Films by Various Concentrations", *J. Microelectron. Electron. Pack.*, 17(1) (2020) 23-27.

[8] O.V. Diachenko et al., "Surface Morphology, Structural and Optical Properties of MgO Films Obtained by Spray Pyrolysis Technique", *Acta Phys. Pol. A*, 3(130) (2016) 805-810.

[9] M. Fathi, M. Ghasemifard and E. Fathi, "Determination of Optical Constants N and K for MgO Nanopowder Using Kramers-Kronig Equation", *Int. J. Eng. Res. Technol.*, 8(3) (2014) 330-334.

[10] A. Galdikas et al., "Peculiarities of Surface Doping with Cu in SnO_2 Thin Film Gas Sensors", *Sens. Actua.*, 43 (1997) 140-146.

[11] H. Güney and D. Iskenderoglu, "Characterization of MgO:Cd thin films grown by SILAR method", *Can. J. Phys.*, 96 (2018) 804-809.

[12] F.T. Ibrahim, "Characterization of Pulsed-Laser Deposited CuO-Doped MgO Thin Films for Gas Sensing Applications", *Iraqi J. Appl. Phys.*, 3(13) (2017) 13-17.

[13] M. Ikram et al., "Graphene Oxide-Doped MgO Nanostructures for Highly Efficient Dye Degradation and Bactericidal Action", *Nanoscale Res. Lett.*, 16(56) (2021) 1-11.

[14] J.Y. Kim, H.S. Jung and K.S. Hong, "Effects of Acetic Acid on the Crystallization Temperature of Sol–Gel-Derived MgO Nano-Powders and Thin Films", *J. Am. Cer. Soc.*, 88(3) (2005) 784-787.

[15] M.S. Mastuli et al., "Effects of Lithium Dopant on Size and Morphology of Magnesium Oxide Nanopowders", *Malaysian J. Anal. Sci.*, 1(18) (2014) 15-20.

[16] Z. Mohammed, S. Khalil and M. Mutter, "Synthesis and characterization of ZrO_2:MgO thin films by plasma of R.F. magnetron sputtering", *Karbala Int. J. Mod. Sci.*, 1(5) (2019) 11-18.

[17] R. Murugan et al., "Magnesium oxide nanotubes: synthesis, characterization and application as efficient recyclable catalyst for pyrazolyl1,4-dihydropyridine derivatives", *Tetrahedron*, 35(68) (2012) 7196-7201.

[18] B.G. Obeid, A.S. Hameed and H.H. Alaaraji, "Structural and Optical Properties of TiO_2:MgO Thin Films Preparing at 373K", *Digest J. Nanomater. Biostruct.*, 4(12) (2017) 1239-1246.

[19] A. Patterson, "The Scherrer formula for X-Ray particle size determination", *Phys. Rev.*, 56(10) (1939) 978-982.

[20] T. Serin et al., "Electrical, structural and optical properties of SnO_2 thin films prepared by spray pyrolysis", *J. Noncryst. Solids*, 352(3) (2006) 209-215.

[21] H. Shokry Hassan et al., "Synthesis, Characterization and Fabrication of Gas Sensor Devices Using ZnO and ZnO:In Nanomaterials", *Beni-Suef Univ. J. Basic Appl. Sci.*, 4(4) (2014) 1-6.

[22] S.-Q.B. Sun, W. Zhang and D. Wang, "Preparation and antibacterial activity of Ag–TiO_2 composite film by liquid phase deposition (LPD) method", *Bull. Mater. Sci.*, 31(1) (2008) 61-66.

[23] S. Suresh, "Investigations on Synthesis, Structural and Electrical Properties of MgO Nanoparticles by Sol-Gel Method", *J. Ovonic Res.*, 6(10) (2014) 205-210.

[24] M.S. Wagh et al., "Preparation of MgO Nanostructure Powder by Sol-gel Method", Int. J. Chem. Phys. Sci., 4 (2015) 115-117.

[25] D. Wojcieszak et al., "An impact of the copper additive on photocatalytic and bactericidal properties of TiO_2 thin films", *Mater. Sci. Poland*, 35(2) (2017) 421-426.

 © All Copyrights are reserved

Studying Effects of Thickness and Temperature on Performance of Pervoskite-Based Solar Cells

Dhuha E. Tareq, Fouad A. Senaed, Ahmad. A. F.

Alayen University, Nasiriyah, IRAQ

Abstract
The photovoltaic research community has focused heavily on organic-inorganic perovskite solar cells recently, making them a superior alternative to other solar cell components. Organometal halide perovskites are regarded to be promising materials for light-emitting devices and have recently attracted a lot of attention. Organometal halide perovskites have been used as absorbent materials in the development of solar systems with efficiencies more than 20% in recent years. A planar hetero-junction perovskite-based solar cell's conventional structure consists of a back electrode, hole transport material (HTM), perovskite absorber, and electron transport material (ETM),and transparent electrode. Device performance has been shown to be significantly impacted by the HTM's hole mobility and acceptor concentration, interface trap density, and back contact metal's work-functio. All these characteristics as well. This study used ETM (SnO_2) with the perovskite CH3NH3PbBr3 and found that the combination of SnO_2 and perovskite produced a high efficiency of 41.23%.

Keywords: Tin dioxide; Solar cells; Perovskite solar cells; Organometal halides; Electron transport material
Received: 2 July 2020; **Revised:** 5 August 2020; **Accepted:** 12 September 2020; **Published:** 1 October 2021

1. Introduction

Simple production procedure of $CH_3NH_3PbX_3$ compounds and substantially improving photoelectric conversion efficiency (PCE), which increased from 3.81% in 2009 to 22.1% in 2016, make them promising candidates for future applications [1-2]. Perovskite solar cells based on $CH_3NH_3PbX_3$ have recently attracted a lot of attention. It is vital to research the equilibrium between carrier diffusion length and thickness in perovskite thin films in order to produce high-performance devices. While the perovskite absorption layer's ability to absorb light can be improved by increasing thickness. Due to restrictions in the light-harvesting electron and hole diffusion lengths, the related perovskite solar cell's PCE is not always improved by perovskite absorption layers. Additional advantages of perovskite include its high carrier transmission capacity, high absorption coefficient, easy manufacturing at low temperatures, and low sensitivity to crystal flaws, which increased in the likelihood of PCE solar cells being produced absorbers by around 20% [3, 4].

In structures of perovskite with the general formula ABX_3 (X is carbon, oxygen, nitrogen, or halogen), the cation is filled on a cubooctahedral site, while the B cation is occupied on an octahedral site (Fig. 1). When used with O_2 anion, the elements A and B are frequently divalent and tetravalent. On the other hand, monovalent and divalent cations can be used at sites A and B when perovskites containing halogen anions are present. The A-site cation in $CH_3NH_3PbI_3$ is $CH_3NH_3^+$, and the B-site cation is Pb^{2+}, as shown in (Fig. 2b). The formability of perovskite is determined using the geometric tolerance factor (t) [7], $t = (r_A+r_X)/[H_2(r_B+r_X)]$, where the effective ionic radii for ions A, B, and X are, respectively, r_A, r_B, and r_X. A perfect cubic perovskite is anticipated for transition metal cations that make up oxide perovskite when t=1, however an octahedral distortion is observed at t=1 [8].

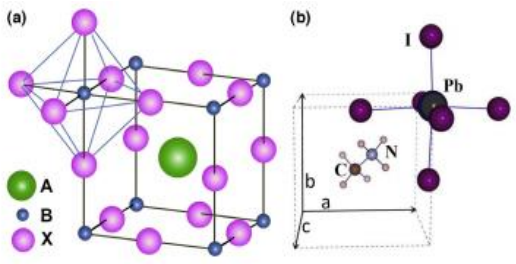

Fig. (1) (a) the structure of the perovskite ABX3 with the larger A cation occupied in the Cubo octahedral position and the BX6 octahedral structure. (b)show A cubic perovskite unit cell made of $CH_3NH_3PbI_3$. The first image in (b) was lifted from Ref. [9]

 © All Copyrights are reserved

Burgelman et al. have developed the SCAPS 1D simulator by solving basic semiconductor device equations in a stable environment [10] to thin film heterojunction solar cells' electrical properties in a model. It was used in this study to examine how a real solar cell ($MASnI_3$) device performed with various material parameters. Both interface defect recombination and deep bulk level defect recombination are supported by the program (non-radiative recombination). Radiative (direct band-to-band recombination) and interface recombination account for a sizable portion of the system's recombination losses, which are counterbalanced by Shockley-Read-Hall recombination (propagated by defects or traps). The flow chart below shows the steps involved in SCAPS simulation.

Radiative recombination (direct band-to-band recombination) and interface recombination account for a sizable portion of the recombination losses in the system under consideration, which are balanced by Shockley-Read-Hall recombination (propagated by defects or traps). Figure (2) shows a flow chart of the SCAPS simulation's stages in detail [11,12].

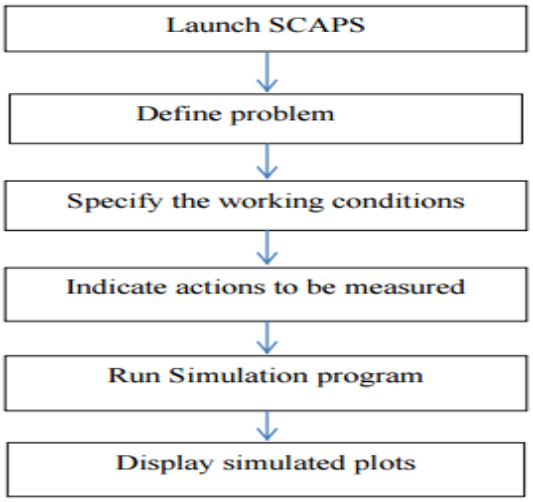

Fig. (2) Simulation procedure

It's important to note that the simulation parameters for the architecture's layers were selected with consideration for existing experimental results and relevant research [14]. The main variables of the simulation are listed in Table (1).

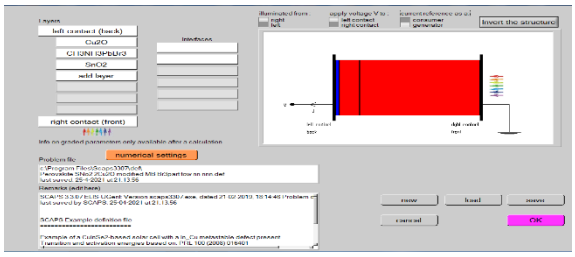

Fig. (3) Heterojunction solar cells made of $C_2uO/CH_3NH_3PbI_3/TiO_2$, $C_2uO/CH_3NH_3PbBr_3/ZnO$ on a SCAPS panel

Table (1) The ETM composition , the absorber, and the HTM [15-16]

Parameters	Cu_2O	$CH_3NH_3PbBr_3$	SnO_2
Band gap (ev)	2.17	2.33 [18]	3.5
Effinity of Electron (ev)	3.20	3.70 [19]	4
Electrical conductivity	7.11	7.50 [21]	9
CB state-effective density ($1/cm^2$)	2.02E+17	1.00+17 [21]	4.300E+18
VB state-effective density ($1/cm^2$)	1.10E+19	1.00+17 [21	2.500E+19
Mobility of electron ($cm^2/v.s$)	2.000E+2	24 [22]	1.000E+7
mobility of hole ($cm^2/v.s$)	8.00E+18	24 [22]	1.000E+7

2. Discussion

To absorb the majority of photons and produce electron-hole pairs, the absorber layer should be adjusted to the appropriate thickness. The absorber layer is now 0.7 μm thick, up from 0.05 μm. The longer illumination wavelength will result in a significant amount of electron-hole pair generation as the absorber layer becomes thicker. The depletion layer closely resembles the back contact and draws additional electrons for recombination as the absorber layer thickness is increased . Less electrons will be used in the generating process as a result, which will impair efficiency and lower the filling factor. As the thickness of the absorber layer rises, PV characteristics change as shown in Fig. (4). The graph of V_{OC} versus thickness suggests that increasing thickness raises V_{OC}. The J_{SC}/thickness graph shows that I_{SC} decreases as circuit thickness increases. The statistics for the drawings are shown in tables (2) and (3).

A product's performance is significantly influenced by its working temperature. The normal testing temperature for a solar cell device is 300 K. As demonstrated in Fig. (5), when the operating temperature was raised

 © All Copyrights are reserved

from 213 to 333K, the characteristics also altered. The J_{SC}, FF, and fall from 45.95 to 45.91 mA/cm^2, 65.98 to 49.73% and 32.71 to 26.40% when the temperature is elevated from 213 to 333 K, whereas V_{OC} increased by 1.07 to 1.15%. Greater stress and deformation brought on by higher temperature can result in more interfacial flaws and less effective layer interconnectivity.

Table (2) Create parameters for the study of numbers

left contact electrical properties (Pt)	
Atomic emission of heat / Recombination on the surface electron Velocity (cm/s)	10^5
Atomic emission of heat / recombination on the surface Velocity of hole (cm/s)	10^7
Metal (Pt) work function (ev)	5.65
Right contact electrical properties	
Thermionic emission / recombination on the surface electron Velocity (cm/s)	10^7
Thermionic emission / recombination on the surface hole Velocity (cm/s)	10^5
ITO work function (ev)	4.4

Table (3) variation of $CH_3NH_3PbBr_3$ thickness with device parameters

Thickness(µm) $CH_3NH_3PbBr_3$	V_{OC} (V)	J_{sc} (mA/cm^2)	F.F (%)	η (%)
0.03	3.66	36.84	11	14.86
0.04	3.36	36.68	10.30	12.72
0.05	2.87	36.49	10.16	10.85
0.06	2.46	36.24	9.71	8.68
0.07	2.17	35.88	8.77	6.84
0.08	1.96	35.20	7.49	5.18
0.09	1.81	33.74	6.12	3.74

The characteristics of the $Cu_2O/CH_3NH_3PbBr_3/SnO_2$ heterojunction solar cells

Temperature (K)	Voc (volt)	Jsc (mA/cm^2)	FF	Efficiency%
213	1.07	45.95	65.98	32.71
233	1.08	45.94	64.19	32
253	1.09	45.94	62.44	31.30
273	1.09	45.93	60.63	30.58
293	1.1	45.92	58.34	29.67
313	1.12	45.92	54.73	28.28
333	1.15	45.91	49.73	26.40

When defect density increases, there is an increase in recombination and a decrease in diffusion length. Device efficiency decreases as a result of the changing band gaps, carrier mobility, and electron and hole concentrations in the materials as a result of the change in resistance brought on by a rise in temperature.

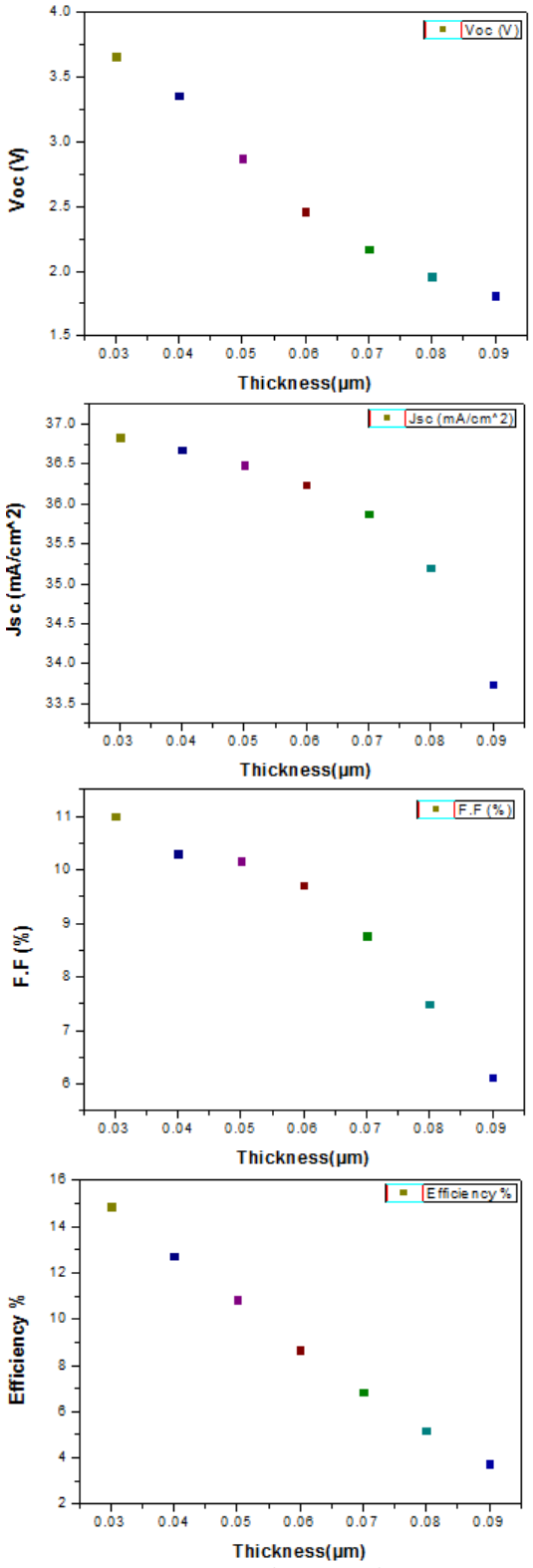

Fig. (4) PV characteristics as functions of the $CH_3NH_3PbBr_3$ thickness

 © All Copyrights are reserved

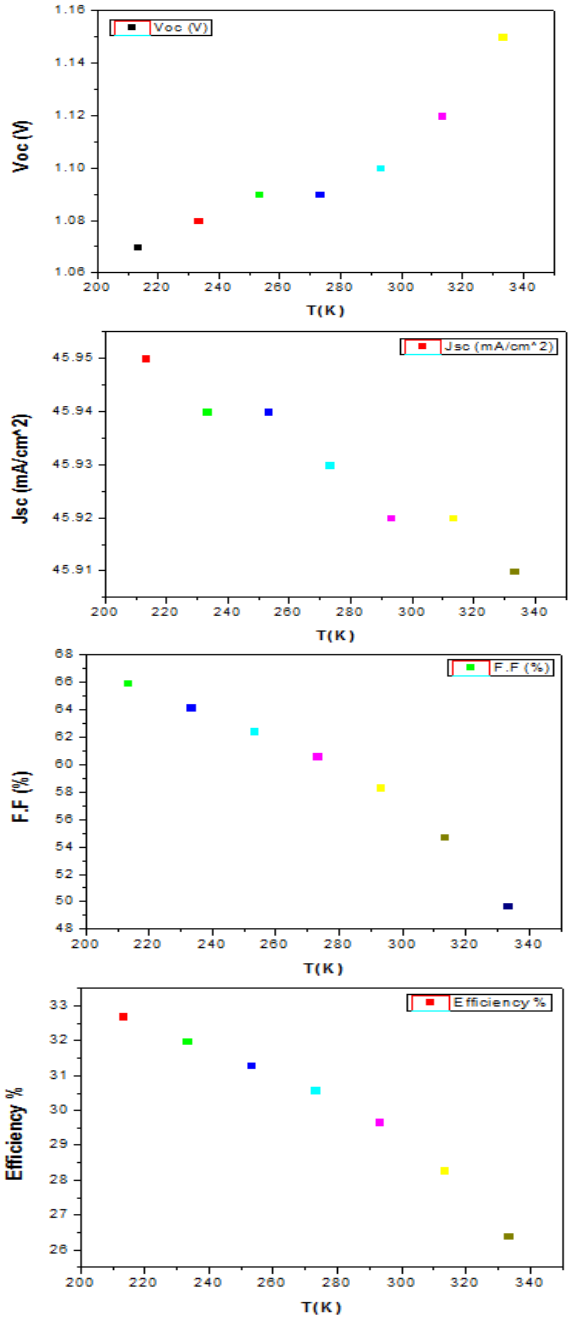

Fig. (5) Solar cell parameters as functions of temperature

3. Conclusions

For each chemical in this study, a change in $CH_3NH_3PbBr_3$, SnO_2 thickness was noted. The study also investigated a wide range of temperature, defect, and work function to identify the ideal parameters that matched to the $Cu_2O/CH_3NH_3PbBr_3/SnO_2$ device's greatest efficiency, which achieved 41.23% at work function 5.12 eV.

References

[1] Y. Wang et al., "Solvent annealing of PbI2 for the high-quality crystallization of perovskite filmsfor solar cells with efficiencies exceeding 18%", *Nanoscale*, 8 (2016) 19654-19661.

[2] M.A. Green et al., "Solar cell efficiency tables (Version 47)", *Prog. Photovolt. Res. Appl.*, 24 (2016) 3-11.

[3] M.J. Taghavi et al., "Modeling of optical losses in perovskite solar cells", *Superlatt. Microst.*, 97 (2016) 424-428.

[4] A. Zhang, Y. Chen and J. Yan., "Optimal Design and Simulation of HighPerformance Organic-Metal Halide Perovskite Solar Cells", *IEEE J. Quantum. Electron.*, 52(6) (2016) 1-6.

[5] D. Bottaro and J. Moscowitz, "Current photovoltaic technology: current progress and future prospects", MIT Energy Lab. Rep.- MIT-EL 77-041W (1977).

[6] W. Shockley and H.J. Queisser, "Detailed balance limit of efficiency of pn junction solar cells", *J. Appl. Phys.*, 31 (1961) 510-519.

[7] V.M. Goldschmidt, "Crystal structure and chemical composition", Ber. Dtsch. Chem. Ges. 60 (1927) 1263–1268.

[8] M. Rini et al., "Control of the electronic phase of a manganite by mode-selective vibrational excitation", *Nature*, 449 (2007) 72-74.

[9] G. Giorgi et al., "Small Photocarrier Effective Masses Featuring Ambipolar Transport in Methylammonium Lead Iodide Perovskite: A Density Functional Analysis", *J. Phys. Chem. Lett.*, 4 (2013) 4213–4216.

[10] M. Burgelman et al, SCAPS manual, no. May. 2014.

[11] A. Niemegeers, M. Burgelman and K. Decock, SCAPS Manual, University of Gent (2014).

[12] T. Minemoto and M. Murata, "Device modeling of perovskite solar cells based on structur- al similarity with thin film inorganic semiconductor solar cells", J. Appl. Phys., 116(5) (2014) 054505.

[13] T.L. Amu, "Performance Optimization Of Tin Halide Perovskite Solar Cells Via Numerical Simulation", Ph.D. thesis, University of Abuja (Nigeria) (2014).

[14] M.I. Hossain et al., "Design optimization of solar cell with molybdenum sulfide as light absorber", *J. Photon. Ener.*, 8(2) (2018) 025501.

[15] C. Wehrenfennig, "Ultrafast spectroscopy of charge separation, transport and recombination processes in functional materials for thin-film photovoltaics", Ph.D. thesis, Oxford University (2014).

[16] M. Nawaz, E.S. Marstein and A. Holt, "Design analysis ZnO/cSi heterojunction solar cell", in Proc. IEEE Photovol. Special. Conf. (PVSC) Honolulu, 20–25 June (2010) 2213–2218.

 © All Copyrights are reserved

Nanoscale Characterization of Green Synthesized Carboxymethyl Cellulose Nanoparticles

Kadhim H. Abdul Sayed, Alaa G. Al-Hasimi, Kareema M. Ziadan

Department of Food Science, College of Agriculture, University of Basrah
Department of Physics, College of Science, University of Basrah

Abstract
This study presents the extraction of cellulose (C) from plant wastes and the preparation of nano-cellulose (NC) using acid hydrolysis and ultrasound method, as well as preparation of carboxymethyl cellulose (CMC) and carboxymethyl nano-cellulose (NCMC) by alkalization and etherification method. Some characteristics of these compounds were studied, including the size of natural polymers, the percentage of yield of nanopolymers, structure and size of polymer nanoparticles measured using AFM, FE-SEM and XRD. The particle size was ranging through 30.90-49.65 nm for NCMC. Three peaks were observed for (C) and (NC) on the diffraction angles of 16.18-16.23, 22.41-22.63 and 34.02-34.76 and crystallization loss for CMC and NCMC.

Keywords: Polymers; Nanocellulose; Carboxymethyl cellulose; Nanoparticles; Toxicity
Received: 2 July 2020; **Revised:** 5 August 2020; **Accepted:** 12 September 2020; **Published:** 1 October 2021

1. Introduction

Cellulose is a water-insoluble polymer because of its high crystallization degree and increased hydrogen bonds between polymer chains, which limits its uses in many food industries [1]. In order to overcome these problems, it is resorted to converting Cellulose to its water-soluble derivatives and common solvents [2]. Where these derivatives obtained through chemical reactions include Carboxymethyl cellulose (CMC), Methyl cellulose (MC), Hydroxypropyl cellulose (HPC), and Hydroxypropyl methylcellulose (HPMC) [3]. CMC is one of the most important straight chain anionic polysaccharides, which is a cellulose ether produced by replacing the hydroxyl groups in the glucose molecule of cellulose with a carboxymethyl group ($-CH_2$-COOH). CMC is prepared from the reaction of cellulose with sodium hydroxide (NaOH) and chloroacetic acid (monochloroacetic acid (MCA)). One of its most important features is that it is odorless, tasteless, and non-toxic, and it is one of the main sources in the preparation of biofilms [4,5]. In addition, CMC has good properties that enable it to form edible and biodegradable films, as well as its ability to carry many natural active ingredients, nutrients, flavors, antioxidants, and antimicrobials [6]. Whereas coatings and films manufactured from CMC are colorless, tasteless, odorless, and hypoallergenic [7]. Acid hydrolysis is a common chemical method in the preparation of nanopolymers [8]. Strong acids are used to break the glycosidic bonds of polysaccharides and wreck the detachment region [9]. As well as the acid attacks the crystalline regions, then the amorphous regions, producing fibers and nanocrystals [10].

Nano cellulose is prepared by acid hydrolysis using concentrated acids such as sulfuric acid, which is one of the most widely used mineral acids [11]. Thus, this reaction process results in nanocrystals charged with a negative charge resulting from the reaction of the acid with the hydroxyl groups of cellulose and also the formation of sulfur groups with a negative charge on the surface of the nanocrystals, which makes them in a state of repulsion and increases their non-agglomeration and ease of isolation and purification [12]. Ultrasound also contributes to an increase in the yield of nanocrystals and an increase in the decrease in their diameter [13,14]. The production of nanoparticles from nano-cellulose derivatives improved the delivery and release of drugs compared to carboxymethyl cellulose in normal size [15].

The study aimed to produce carboxymethyl cellulose nanoparticles from the most

 © All Copyrights are reserved

abundant polymers in nature from agricultural food wastes and study their properties in terms of morphological shape using SEM and AFM Size analyzer.

2. Materials and Methods

Both CMC and NCMC were prepared by two steps:

1- Alkalization pretreatment: Weigh 2 gm of cellulose or nano-cellulose, add 150 ml of isopropanol and 20 ml of (20% NaOH)

2- Etherification reaction: 3.5 gm of monochloroacetic acid was added to the mixture, and 200 ml of ethanol solution was added, and the pH was adjusted to (6-8) using acetic acid. The filtrate was then discarded, and the product was washed three times with ethanol solution and dried at 40°C for 24 hours.

Dimensions of cellulose extracted was measured using Size Analyzer type (90 Plus). The morphology of the polymers was studied using a TESCAN Mira3 field-emission scanning electron microscope (FE-SEM).

The crystallinity of polymers and nanopolymers was measured using an X-Ray Diffraction device (X-Pert pro), with an angle of 2Θ from 10 - 40 degrees. The degree of crystallinity of cellulose, cellulose nanopartiches, carboxymethyl cellulose and carboxymethyl cellulose nanoparticles was calculated according to Eq. (3), The crystallinity index was calculated according to the equation:

$$CrI = (I_{(002)} - \frac{I_{(am)}}{I_{(002)}}) \times 100 \qquad (3)$$

where CrI is the crystallinity index, $I_{(002)}$ is the peak of the crystallization curve at 2θ = 22-26, $I_{(am)}$ is the top of the curve for the amorphous diffraction at 2θ = 15-18.

The average size of the cellulose nanopartiches and carboxymethyl cellulose nanopartiches was measured using an Angstrom AA3000 atomic force microscope (AFM).

3. Results and Discussion

The lower percentages of the yield of carboxymethyl cellulose nanoparticles compared to carboxymethyl cellulose were 37.70 and 26.49% respectively. Figure (1) shows the average size of carboxymethyl cellulose extracted from rice shells, as the figure shows that the average size of natural carboxymethyl cellulose extracted from rice husks was 35.865.7 nm.

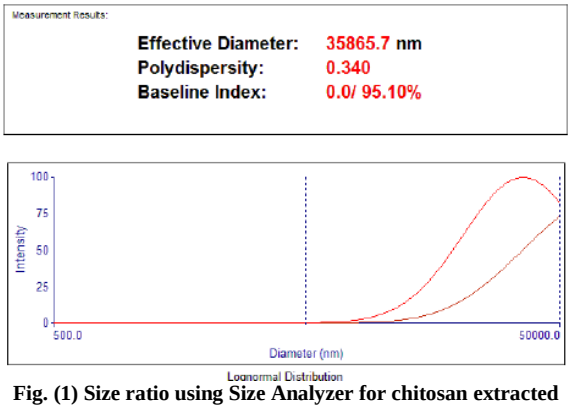

Fig. (1) Size ratio using Size Analyzer for chitosan extracted from shrimp shells and cellulose extracted from rice shells

Figures (2) and (3) show the morphology and diameter of NC and carboxymethyl cellulose (NCMC) nanoparticles prepared from rice husks using FE-SEM to examine the morphology samples. It is noted that the diameters of the cellulose nanoparticles (NC) ranged between 26.77 and 37.29nm, while the diameters of the carboxymethyl cellulose nanoparticles (NCMC) ranged between 30.90 and 49.65nm and irregular spherical shape.

Figures (4) and (5) show the particle size distribution rate of nanocellulose and carboxymethyl cellulose nanoparticles using AFM. The results showed that the minimum size of nanoparticles was about 40 nm, and the size of CMC nanoparticles ranged between 6.53 and 26.17nm and the figure shows the topography of the surface of the CMC nanofilms which have the average roughness 0.906 nm. The reason for the increase in the diameters of the nanoparticles is attributed to the aggregation property of the polymers, especially in the freeze-drying stage, as cellulose nanocrystals can spontaneously assemble due to the formation of hydrogen bonds between the molecules.

 © All Copyrights are reserved

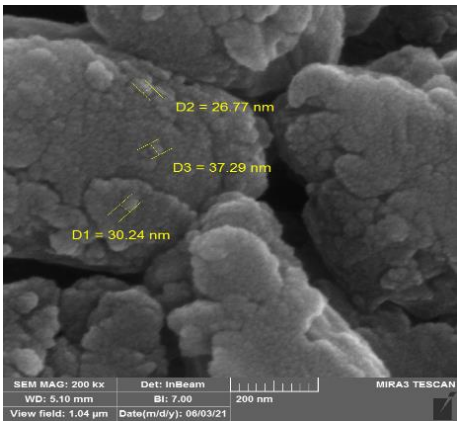

Fig. (2) FE-SEM image of cellulose nanoparticles

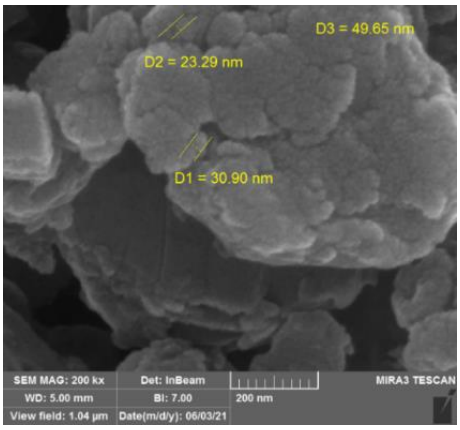

Fig. (3) FE-SEM image of Carboxymethyl cellulose nanoparticles

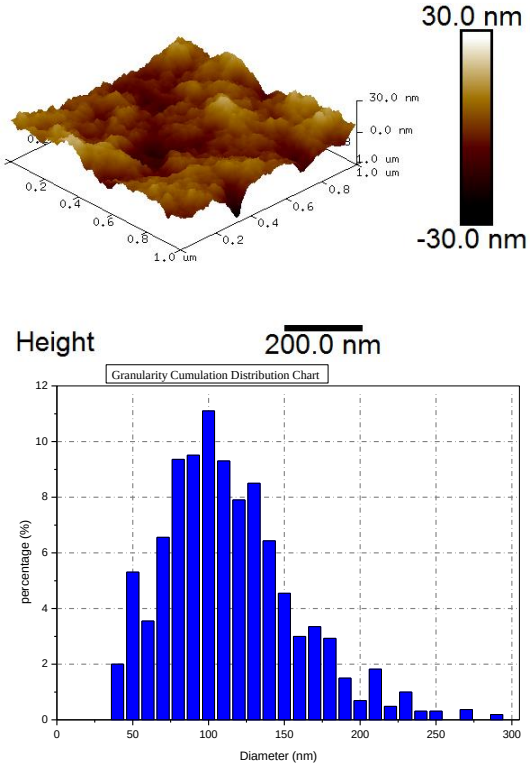

Fig. (4) Dimensions of cellulose nanoparticles using AFM

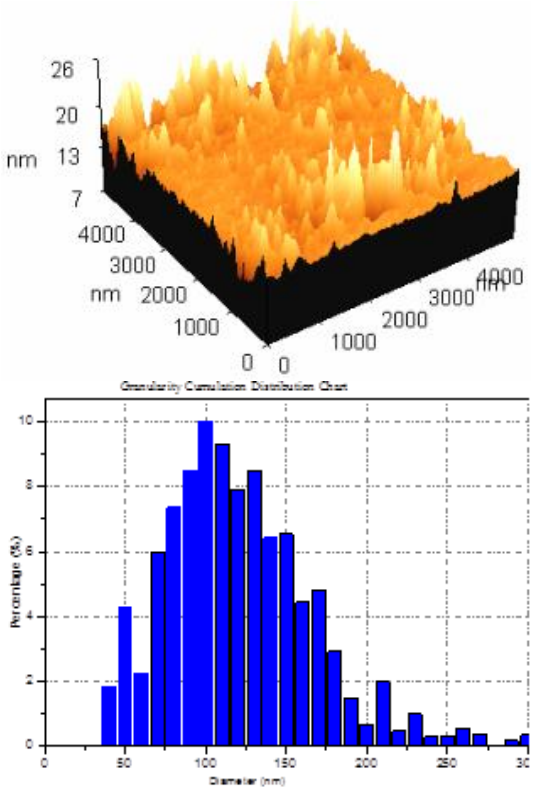

Fig. (5) Dimensions of Carboxymethyl cellulose nanoparticles using AFM

4. Conclusion

Cellulose (C) was extracted from agricultural residues of rice husks and prepared nano-cellulose (NC), Carboxymethyl cellulose (CMC), and Carboxymethyl cellulose nanoparticles (NCMC). The SEM and AFM studies showed that the cellulose nanoparticles Carboxymethyl cellulose nanoparticles were within the nanoscale.

References

[1] Abulkalil, H.P.S., Bhat, A.H., and Yasra, A.F (2012). Green composite from sustainable cellulose naon fibrils:A review. Carbhyd. Polym.J, 87:963-979.

[2] Ali, A., & Ahmed, S. (2018). A review on chitosan and its nanocomposites in drug delivery. International journal of biological macromolecules, 109, 273-286.

[3] Karataş, M., & Arslan, N. (2016). Flow behaviours of cellulose and carboxymethyl cellulose from grapefruit peel. Food Hydrocolloids, 58, 235-245.

[4] Gupta, H., Kumar, H., Kumar, M., Gehlaut, A. K., Gaur, A., Sachan, S., & Park, J. W. (2020). Synthesis of biodegradable films obtained from rice husk and sugarcane bagasse to be used as

 © All Copyrights are reserved

food packaging material. Environmental Engineering Research, 25(4), 506-514.
[5] Singh, R. K. and Singh, A. K. (2013). Optimization of reaction conditions for preparing carboxymethyl cellulose from corn cobic agricultural waste. Waste and Biomass Valorization. 4(1): 129-137
[6] Aljbour, N. D., Beg, M. D., & Gimbun, J. (2019). Acid hydrolysis of chitosan to oligomers using hydrochloric acid. Chemical Engineering & Technology, 42(9), 1741-1746.
[7] Panahirad, S., Dadpour, M., Peighambardoust, S. H., Soltanzadeh, M., Gullón, B., Alirezalu, K., & Lorenzo, J. M. (2021). Applications of carboxymethyl cellulose-and pectin-based active edible coatings in preservation of fruits and vegetables: A review. Trends in Food Science & Technology, 110, 663-673.
[8] Araki, J., Yamanaka, Y., & Ohkawa, K. (2012). Chitin-chitosan nanocomposite gels: reinforcement of chitosan hydrogels with rod-like chitin nanowhiskers. Polymer journal, 44(7), 713-717.
[9] Asri, S. E. A. M., Zakaria, Z., Arjmandi, R., Hassan, A., & Haafiz, M. M. (2017). Isolation and characterization of chitin nanowhiskers from fermented tiger prawn waste. Chemical Engineering Transactions, 56, 139-144.
[10] Bidgoli, H., Zamani, A., Jeihanipour, A., & Taherzadeh, M. J. (2014). Preparation of carboxymethyl cellulose superabsorbents from waste textiles. Fibers and Polymers, 15(3), 431-436.
[11] Chattopadhyay, D. P., & Inamdar, M. S. (2012). Studies on synthesis, characterization and viscosity behaviour of nano chitosan. Research journal of engineering sciences, 1(4), 9-15
[12] Chattopadhyay, DP and Patel, BH (2016). Synthesis, Characterization and Application of Nano cellulose for enhanced performance of textiles. Journal of textile science and engineering 2:248.
[13] Lu, P., & Hsieh, Y. L. (2012). Preparation and characterization of cellulose nanocrystals from rice straw. Carbohydrate Polymers, 87(1), 564-573.
[14] Pandi, N., Sonawane, S. H., & Kishore, K. A. (2021). Synthesis of cellulose nanocrystals (CNCs) from cotton using ultrasound-assisted acid hydrolysis. Ultrasonics sonochemistry, 70, 105353.
[15] Kadry, G. (2019). Comparison between gelatin/carboxymethyl cellulose and gelatin/carboxymethyl nanocellulose in tramadol drug loaded capsule. Heliyon, 5(9), e02404.

 © All Copyrights are reserved

IRAQI JOURNAL OF APPLIED PHYSICS LETTERS
EDITORIAL BOARD

COPYRIGHT RELEASE FORM

IRAQI JOURNAL OF
APPLIED PHYSICS LETTERS (IJAPLett)

We, the undersigned, the author/authors of the article titled

……
……
……
……
……
……
……

that is submitted to the Iraqi Journal of Applied Physics Letters (IJAPLett) for publication, declare that we have neither taken part or full text from any published work by others, nor presented or published it elsewhere in any other journal. We also declare transferring copyrights and conduct of this article to the Iraqi Journal of Applied Physics Letters (IJAPLett) after accepting it for publication.

The authors will keep the following rights:

1. Possession of the article such as patent rights.
2. Free of charge use of the article or part of it in any future work by the authors such as books and lecture notes after informing IJAP editorial board.
3. Republishing the article for any personal purposes of the authors after taking journal permission.

To be signed by all authors:

Signature:……..date: ……
Printed name: ……

Signature:……..date: ……
Printed name: ……

Signature:……..date: ……
Printed name: ……

Correspondence author:……...
……
Address:……
……
Telephone:……..……..email: ……

Note: Complete and sign this form and mail it to the below address with your finally revised manuscript

The Iraqi Journal of Applied Physics Letters
ISSN (Print): 1999-656x, ISSN (Online): 2309-1673
www.iraqiphysicsjournal.com
Email: editor@iraqiphysicsjournal.com
Email: editor_ijap@yahoo.co.uk
Email: ijap.editor@gmail.com

IRAQI JOURNAL OF APPLIED PHYSICS LETTERS
Volume (4) Issue (4) October-December 2021

CONTENTS

The *Iraqi Journal of Applied Physics Letters (IJAPLett)* is a peer reviewed journal of high quality devoted to the publication of original research papers from applied physics and their broad range of applications. IJAPLett publishes quality original research letters in physics and its applications in the broadest sense. It is intended that the journal may act as an interdisciplinary forum for physics and its applications. Innovative applications and material that brings together diverse areas of physics are particularly welcome. IJAPLett aims to disseminate knowledge; provide a learned reference in the field; and establish channels of communication between academic and research experts, policy makers and executives in industry, commerce and investment institutions. IJAPLett is a quarterly specialized periodical dedicated to publishing original letters in: Applied & Nonlinear Optics, Applied Mechanics & Thermodynamics, Digital & Optical Communications, Electronic Materials & Devices, Laser Physics & Applications, Plasma Physics & Applications, Quantum Physics & Spectroscopy, Semiconductors & Optoelectronics, Solid State Physics & Applications, Alternative & Renewable Energy, and Environmental Science & Technology.

Sponsored and Published by
Iraqi Society for Alternative and Renewable Energy Sources and Techniques

Co-published by
American Quality for Scientific Publishing